THE INTERACTIONS OF AND PROTECTION AGAINST HIGH-ENERGY COSMIC RAYS ON EYE TISSUE

An Undergraduate Research Scholars Thesis

by

BRIDGER FREEMAN[1]

Submitted to the LAUNCH: Undergraduate Research office at
Texas A&M University
in partial fulfillment of the requirements for the designation as an

UNDERGRADUATE RESEARCH SCHOLAR

Approved by
Faculty Research Advisor: Dr. Galina Tsvetkova

May 2021

Major: Physics[1]

RESEARCH COMPLIANCE CERTIFICATION

Research activities involving the use of human subjects, vertebrate animals, and/or biohazards must be reviewed and approved by the appropriate Texas A&M University regulatory research committee (i.e., IRB, IACUC, IBC) before the activity can commence. This requirement applies to activities conducted at Texas A&M and to activities conducted at non-Texas A&M facilities or institutions. In both cases, students are responsible for working with the relevant Texas A&M research compliance program to ensure and document that all Texas A&M compliance obligations are met before the study begins.

I, Bridger Freeman[1], certify that all research compliance requirements related to this Undergraduate Research Scholars thesis have been addressed with my Research Faculty Advisor prior to the collection of any data used in this final thesis submission.

This project did not require approval from the Texas A&M University Research Compliance & Biosafety office.

TABLE OF CONTENTS

ABSTRACT

The Interactions of and Protection Against High-Energy Cosmic Rays on Eye Tissue

Bridger Freeman[1]
Department of Physics and Astronomy[1]
Texas A&M University

Research Faculty Advisor: Dr. Galina Tsvetkova
Department of Nuclear Engineering
Texas A&M University

As the interest in space exploration becomes ever more relevant, so too do the health risks of space. For humans, the eyes are one of the most vulnerable organs to radiation. Though there is notable previous research that explored the holistic effects of cosmic rays on the body, much of this research either exclusively considered low-weight ions, which are far more common due to lower-energy solar radiation, or it analyzed dose-dependent, pathological effects such as cataracts or cancer. In this work, the Transport of Ions in Matter (TRIM) software was used to analyze the interactions, range, and damage that incident nuclei inflict on exposed eye tissue at 20 MeV, 1 GeV, and 10.08 GeV. This software simulated the interactions that high-energy, galactic cosmic rays would have on an astronaut's eyes. Through this, an in-depth analysis of the way that high-energy cosmic rays interact with the eyes of astronauts in space was performed to better understand the relationship between nuclear mass and range, ionization, straggling, the energy loss of incident ions, and tissue damage. The efficacy that practical, high-density polycarbonate and metal shielding has on protecting the eye from these incident ions was also tested. It was found that though the gold-coated polycarbonate visor was effective at protecting against lower-energy or heavier particles, it was ineffective at shielding against high-energy cosmic rays above 1 GeV. However, mere millimeters of lead and aluminum were found to effectively shield a vast majority of the

damage from these incident particles. It was suggested that recent advancements in head-mounted devices such as virtual-reality headsets may permit the utilization of this radiation shielding while overcoming obstruction to visibility that may have otherwise been an issue.

DEDICATION

To my family, faculty advisor, and peers who supported me throughout this research project.

ACKNOWLEDGMENTS

Contributors

I would like to thank my faculty advisor, Dr. Galina Tsvetkova, for her guidance and support over the course of this research project.

A special thanks also goes to my friends and colleagues, in addition to the faculty and staff of Texas A&M, for making my time at the university such a wonderful experience.

The software used for The Effects of and Protection Against High-Energy Cosmic Rays on Eye Tissue was provided by James Ziegler and Jochen Biersack, who developed it.

All other work conducted for the thesis was completed by the student independently.

NOMENCLATURE

SRIM	Stopping Range in Matter
TRIM	Transport of Ions in Matter
TAMU	Texas A&M University
GCRS	Galactic Cosmic Ray Simulator
eV	Electron Volt
MeV	Mega-Electron Volt, i.e., 10^6 eV
GeV	Giga-Electron Volt, i.e., 10^9 eV
Z	The Number of Protons in a Nucleus: Atomic Number
GCR	Galactic Cosmic Rays
LET	Linear Energy Transfer
NASA	The National Aeronautics and Space Administration

1. INTRODUCTION

The advancement of human space exploration has become an increasingly relevant topic in today's world. From revolutionary rocket designs to permanent lunar stations to mars habitation, mankind has its eyes set on the stars as it works effortlessly to establish a presence away from planet Earth. Though it may seem obvious that staring at the sun can readily cause eye damage, it is less obvious that invisible radiation from distant stars and galaxies can also cause lasting damage to the unprotected eyes of those venturing out of Earth's atmosphere. These effects were eventually noticed and studied, ultimately leading to the conclusion that there is a significant association between high-inclination or lunar missions and the development of cataracts, likely from the increased heavy-ion flux [1]. A cataracts prevalence of 13.6% was found in astronauts who participated in the Longitudinal Study of Astronaut Health [1]. A report on the ophthalmological risks of space travel indicates that exposure to high-LET GCRs, especially iron, is correlated with this development [2]. Though these studies explore the existence and cause of eye damage for those traveling into space, they refrain from investigating the way that high-LET GCRs interact with the eye. To contribute to the understanding of the way that these rays interact with the eye in an effort to better protect the eyes of current and future astronauts, this project modeled and quantified the range and damage of high-energy, heavy-ion cosmic rays on the human eye. Additionally, an in-depth analysis of the interactions of these ions with the human eye was performed. Following this, various practical shielding materials were presented, and their efficacy at shielding against these GCRs was studied. The conclusions drawn from this study allowed for the recommendation of a more effective shielding design for astronaut helmets, which would significantly reduce the damaging effects that high-LET cosmic rays have on the eyes of those traveling in space.

2. METHODS

2.1 Transport of Ions in Matter [TRIM]

The primary tool used to analyze the interactions of nuclei with the tissue in the eye was the Transport of Ions in Matter (TRIM) software. This software is based on Monte Carlo simulations, which refer to a broad class of computational algorithms dependent on repeated random samples to yield numerical results. According to an article published by Ziegler and Biersack, who developed SRIM and TRIM, this software outputs the distributions of incident ions in target compounds by primarily using Bragg's rule and then employing the "Köln Core and Bond approach" to make corrections between Bragg's rule and compounds containing specific elements that have a large bonding effect on stopping powers [3]. For high energy, heavy ions, the software utilizes the Brandt-Kitagawa approximation is used to address the charge of these particles and the Bethe-Bloch stopping equation [3]. By simulating thousands of ions of an element at a given energy level, the TRIM software provides a numerical approximation of several parameters of interest, including incident particle range, damage per ion, target ionizations, ionizations per incident ion, and sources of energy loss through analysis of the interactions as each ion passes into and interacts with the tissue.

2.2 Cosmic Rays

Cosmic rays consist primarily (>98%) of atomic nuclei [4]. These rays can range in energy from a few MeV to well over 10^{20} eV [5]. Of these, only hydrogen (Z=1) through lead (Z=82) have ever been observed. The remaining fraction of cosmic rays consists of electrons, muons, and other sub-atomic particles. Of the atomic nuclei in cosmic rays, the cosmic ray flux consists of approximately 85% protons, 12% alpha particles, and only 1% of heavier elements [5]. To go a step further, Beatty, Matthews, and Wakely [6] found that the intensity of primary nucleons at an energy of a few GeV to beyond 100 TeV can be estimated by a relation where the intensity is inversely proportional to the energy of the nucleon, including rest-mass energy. This means that there are dramatically fewer cosmic rays observed as the nuclear mass increases and as the energy

of the particle increases. This makes sense, considering how these particles are created. High-energy, heavy cosmic rays are produced in high-energy cosmic events, such as the collision of galaxies, supernovae, and to a lesser degree, solar flares. However, in order for very heavy cosmic rays to be produced, a very specific set of conditions must be met, relating to the mass of the star in question and the energy of the event. Because of this, high-energy cosmic rays heavier than iron can be incredibly rare. However, their existence has been observed, and this project works to quantify their interactions with and damage on the exposed eye, in addition to the eye protected by shielding.

2.3 Experimental Design: Part 1 - Interactions with Eye Tissue

Because only ions of hydrogen up to lead have ever been observed in cosmic rays, this experiment is bounded by the range of elements from Z=1 to Z=82. TRIM calculations lose a significant degree of accuracy for energy levels above 10.00 GeV per amu, as TRIM's algorithms rely on approximations that prove highly inaccurate for particles with energy greater than this. In order to have a standardized level of analysis, all ion simulations for the highest energy group were analyzed at the maximum energy level for hydrogen, 10.08 GeV. To explain the interactions of nuclei across the cosmic ray energy spectrum, three energy levels were tested: 20.00 MeV, 1.00 GeV, and 10.08 GeV. Fluctuations across all TRIM calculations were found to universally reach equilibrium well before 5000 ions simulated per run. Because of the nature of the Monte Carlo simulations, the accuracy of the final output increases with increased ion simulations per trial. For this reason, 5000 ions were simulated per ion for the 20.00 MeV and 1.00 GeV trials. However, because the time and computational power required to simulate each ion interaction significantly increase with nuclear mass and particle energy, simulating 5000 ions per element was impractical at 10.08 GeV. Several ions were chosen from the range of elements tested at 10.08 GeV and the results from 5000 ions simulated were compared to the results from 1000 ions simulated. Because the differences were less than 0.1% at a maximum, the 10.08 GeV trials were conducted using only 1000 ions per element.

2.3.1 Model of the Human Eye

Because TRIM simulates particles penetrating into a 2-Dimensional material, the practical way to design a cosmic ray interacting with maximal impact is to design a replica of the eye that has been sliced through the cornea along the sagittal plane. Due to the inherent minute differences in the chemical composition between adjacent layers, a simplified model of the eye was used for calculations. This simplified model included major eye structures, and it combined those layers with less than 0.5% difference in chemical composition and less than 50 microns difference in thickness into one layer. The exact dimensions of this model are detailed in Appendix A.

2.3.1.1 Limitations to a Flat-Eye Model

Since the target material's dimensions were only able to be established in a way that resulted in a flat surface, this model was limited by the physical curvature of the eye. More specifically, the difference in path length that a cosmic ray will experience when interacting with the eye at any point off-center was not able to be accounted for in the flat-eye model. Because of this limitation, this project explored the interactions of ions that have ranges that fall within the longest path length, as measured from the center of the cornea, orthogonal to the skull, and directly back to the macula, when measured parallel to the transverse plane, which has a standard thickness of approximately 23 millimeters. For clarification, consider the following example: The cornea has a standard radius of curvature of 7.80 millimeters [7]. If a ray were to impact the eye at a distance of "x" away from the center of the cornea and orthogonal to the face, the ray would now effectively observe the radius shortening by an amount equal to the radius of curvature times the cosine of the angle formed by the center of the eye and the point where the ray intersected. If, for example, this distance "x" was 5 millimeters, then the shortening of the eye thickness for a ray approaching normal to the skill would be approximately 1.98 millimeters. This would be an extreme case, since the human cornea has an average diameter of 11.5 millimeters. In contrast, the retinal tissue has an average radius of curvature of approximately 12 millimeters. This same displacement in collision coordinate from the center of the eye would constitute approximately a 3.26 millimeters difference in radius length

or approximately 6.52 millimeters in eye thickness for a ray passing directly through the eye and orthogonal to the skull.

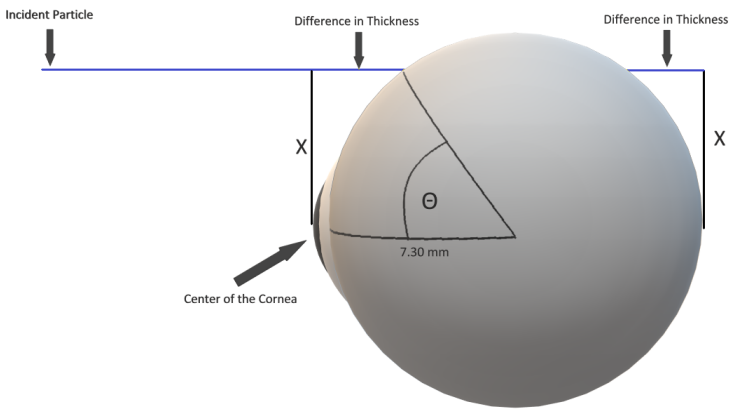

Figure 2.1: Limitations of Flat Eye Model

2.4 Experimental Design: Part 2 - Shielding

2.4.1 Astronaut Helmet Shielding

To test the efficacy of current astronaut helmet designs at shielding the eye from high-energy cosmic rays, two additional layers, one of gold and one of polycarbonate plastic, were added to the front of the eye model described in Section 2.3.1. Astronaut helmets are equipped with a polycarbonate plastic helmet visor, which is coated in a thin layer of gold. This gold coat is approximately 500 Angstroms thick, and the polycarbonate shield is 5 millimeters thick [8]. The polycarbonate structure serves to provide mechanical protection to the astronaut's face. The gold layer serves to deflect much of the solar radiation, aiding in the thermal control of the spacesuit [9]. The metal layer cannot be much thicker than this, since at 1,000 angstroms, essentially no light can pass through, rendering the visibility through the visor entirely null. The existence of gasses between the eye and the polycarbonate plastic layer was not accounted for, as they have negligible effects on attenuating high-energy cosmic rays across short distances. In this set of trials, this model was subject to the same simulations detailed in Part 1 for 20.00 MeV, 1.00 GeV,

and 10.08 GeV. All parameters studied in Part 1 were compared to the values obtained in these trials, and those with significant changes ($\Delta < 1.0\%$) were recorded for further analysis with different shielding, including damage per incident ion and range.

2.4.2 Newly Designed Shielding

Following the trials using the standard astronaut helmet design, the efficacy of platinum, tungsten, and lead were tested at 500 angstroms on top of the polycarbonate shield and compared to gold. These three were chosen as primary candidates for radiation shielding due to their density and documented capacity for absorbing nuclear radiation. It was found that there were negligible differences in the efficacy of each metal at shielding against cosmic rays for the aforementioned energy levels tested, though gold typically proved marginally most effective. To produce a cost-effective solution to cosmic radiation shielding, lead was selected as the primary candidate to be tested in a thicker radiation shield design. This new design included an outer 5-millimeter layer of polycarbonate plastic, which was selected for its ability to provide structural integrity from mechanical damage to the helmet, in addition to its moderate effectiveness at absorbing radiation in the trials in Section 2.4.1. Following the polycarbonate plastic layer, a 3 millimeter thick lead shield was used, with the primary function of radiation absorption to increase the rate of particle attenuation, limiting interaction with the eye. The thickness was chosen due to concerns about the extra weight that lead shielding adds to the helmet. Because lead adds several pounds to the weight of the helmet per millimeter of thickness in plating (assuming a hemispherical lead plate), three millimeters of thickness was chosen as an appropriate ratio of weight to shielding added. Finally, an inner layer of aluminum, 3 millimeters thick, was added to the inside of the lead plating. This aluminum plate served the primary function of limiting lead exposure to the astronaut within the helmet. In addition, the aluminum added a layer of protection from mechanical damage and a small amount of radiation shielding prior to contact with the eye. Again, the existence of gasses between the exposed eye and this shield was not accounted for. The exact details of this design are found in Appendix B. Though this helmet design does not allow for the direct transmission of light for visibility, it was assumed that the advances in virtual reality headsets may be incorpo-

rated into this helmet design. This would incorporate a digital display on the inside of the helmet connected to a video camera outside the helmet, allowing for visibility. The shielding provided by this display was not accounted for in this experimental design. This polycarbonate plastic, lead, and aluminum shielding design, followed by the model eye from Section 2.3.1, was subject to the same simulations for each element as in Part 1, at 20.00 MeV, 1.00 GeV, and 10.08 GeV. After this, the astronaut helmet shielding from Section 2.4.1 and the shielding from this section were tested separately, without the eye model, for elements Z=1 to Z=82 and at 20.00 MeV, 1.00 GeV, and 10.08 GeV. This allowed the software to quantify how much damage was absorbed in the shielding alone. These values were then compared to the damage from the respective trials where the shielding and eye model were tested together, allowing the damage per ion transmitted to the eye with each type of shielding to be quantified and compared to the damage without shielding. In this way, the efficacy of each shielding type was quantitatively measured, and the best shielding type was determined.

3. ANALYSIS AND RESULTS

Using the methods described in Section 2, the following parameters were analyzed: the longitudinal and radial range of incident particles into the eye and beyond, straggling for these parameters, total ionization per ion, total phonons per ion, total target damage per ion, number of vacancies or displacements per ion, and the fraction of ion energy lost to each of these. This data was then compared to the results from both sets of shielding trials, with particular attention paid to the differences in damage per incident ion and range of incident particles into the target material. The following discussion summarizes the significant findings from this set of experiments.

3.1 Layers of the Eye and Shielding Legend

The following legend is used throughout the remainder of this report to identify the layers on each range graph. Each number corresponds to its respective layer of the eye or shield.

Layer	**Thickness** (μm)	**Color/Number**
Cornea	53.4	1
Anterior Chamber	2,570	2
Lens	4,830	3
Iris	430	4
Vitreous Body	15,170	5
Retina	265	6
Choroid	280	7
Sclera	650	8
Brain	150,000	9
Skull	7000	10
Through the Head	N/A	11
Gold	0.05	12
Polycarbonate Plastic	5,000	13
Lead	3,000	14
Aluminum	3,000	15

3.2 Radiation Without Shielding

3.2.1 Penetration Range of Incident Ions

The following graph represents the dependence of the range on a nuclear mass of incident ions with different energies.

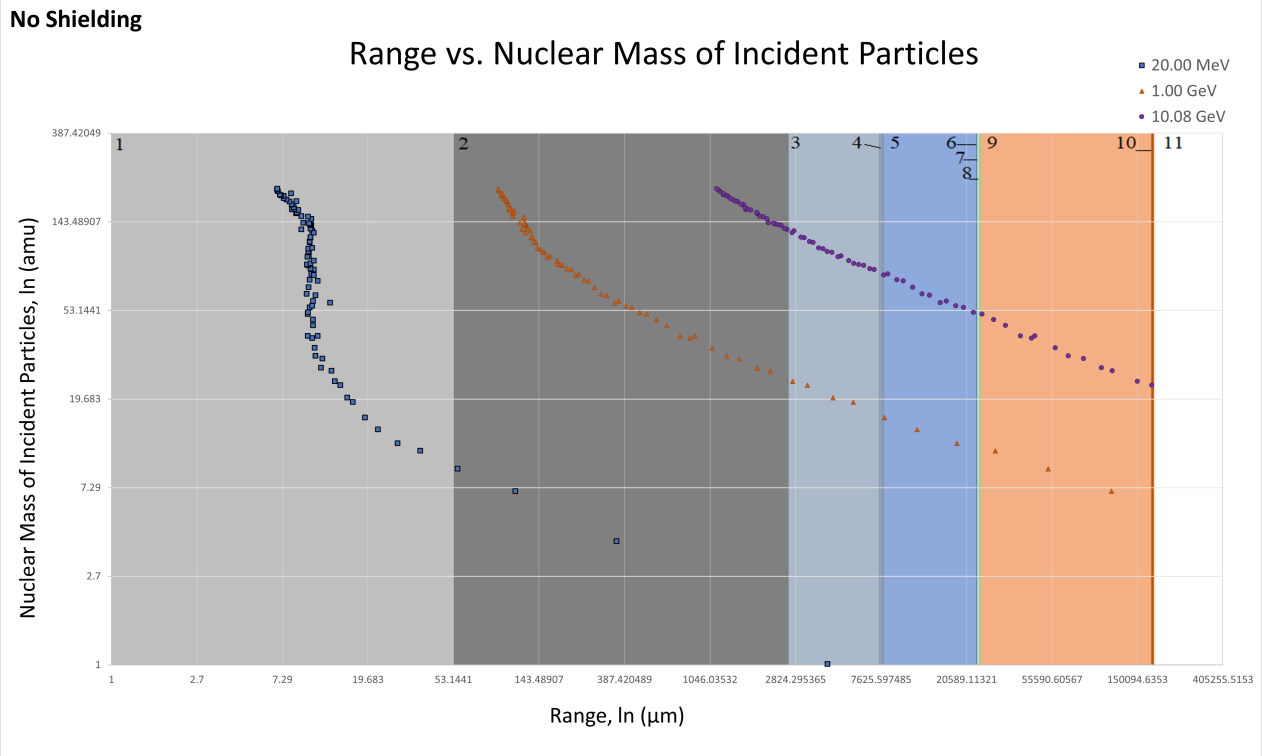

Figure 3.1: Incident Particles Penetrating the Unshielded Eye, Range Data

It was found that ions with higher energies traveled considerably farther into the eye than those with lower energies. For example, at 20 MeV iodine traveled 10.5 microns into the cornea. However, at 1.0 GeV iodine traveled 123 microns into the eye, passing completely through the cornea and into the anterior chamber. Likewise, at 10.08 GeV iodine traveled 2.72 millimeters into the eye, passing through the cornea and the anterior chamber before coming to rest in the lens of the eye. It was noted that for 1.00 GeV and 10.08 GeV, several low-weight particles passed

completely through the eye and came to rest in the brain or skull. Several lightweight particles passed completely through the head. The particles that passed through the head had indeterminate ranges. This is because the range once a particle passed out of the skull depends on the gasses or shielding behind the head of the astronaut, which are beyond the concerns of this experiment. As a consequence of this factor, the ions that pass through the head are not included on any range graphs.

3.2.1.1 Range Analysis

By analyzing the nuclear mass verses the projected longitudinal range, a clear relationship was observed between the two. A linear relationship between the natural log of the nuclear mass and the natural log of the longitudinal range was found. The strength of this linear trend was increasingly more accurate as the energy level of the incident ions increased, having a R^2 >0.95 at energies above 1.0 GeV. When analyzing the fraction of incident ion energy lost at each level, it was determined that up to 22.65% of ion energy was lost to recoil ionizations at 20.00 MeV. Heavier particles suffered significantly more energy loss to recoil ionizations than lighter particles. At 1.00 GeV, a maximum of 1.07% of incident particle energy was lost to recoil ionizations, and at 10.08 GeV the maximum was 0.15%. For lower energy incident ions, the linear dependence was observed. This dependence was strong for particles with heavier nuclear masses and deviates significantly from linear fit in the higher-energy counterparts. This effect can be explained by the fact that more energy was lost to recoils at lower ion energies. Using this dependence, the expected range for the incident ion that shows how far it will penetrate the eye can be calculated as a function of the nuclear mass of the incident ions. The accuracy of these calculations increases significantly for higher energy particles. They are also more accurate for calculations involving lighter particles since these were found to have minimal energy loss to recoils. This observation is shown in Figure 3.2. The residuals for ions at 10.08 GeV have the most reliable trend line, with an R^2 value of 0.9958. The residuals do not reveal any significant error trends with the calculations performed.

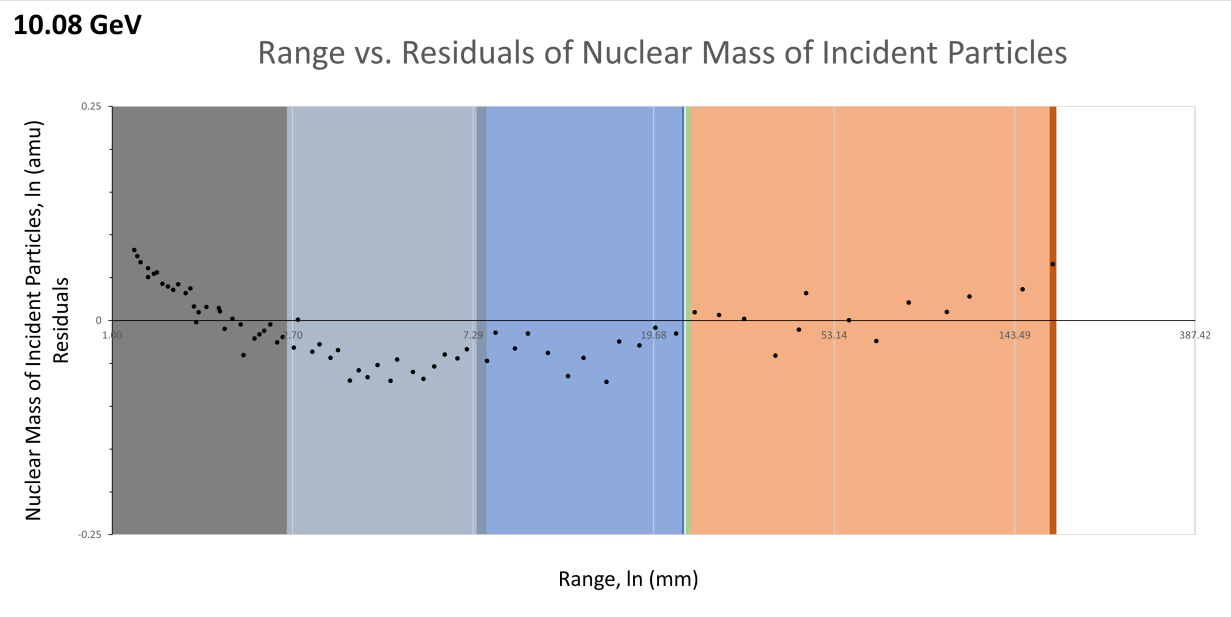

Figure 3.2: Incident Particles Penetrating the Eye, Range Data Residuals - 10.08 GeV

Because a linear trend was observed of a log-log graph of the range verses the nuclear mass of incident ions, the relationship between the two can be approximated by the following equation:

$$\text{Nuclear Mass} = K(\text{Longitudinal Range}^n) \qquad \text{(Eq. 1)}$$

where K is a constant and n is the exponential order of the relationship. Figure 3.1 shows that the trend line for each energy level tends towards a constant slope, especially for lighter particles. However, each data set has its own set of constants for the range as a function of nuclear mass. From the three energy levels tested, the 10.08 GeV data has the strongest linear fit, with an R^2 value of 0.9958. To illustrate how the K and n constants can be garnered from the experimental value, consider the following. Let M be the nuclear mass in amu and R be longitudinal range in millimeters. By simple conversion from exponential to linear form, Eq. 1 becomes Eq. 2:

$$\ln[R] = n * \ln[M] + \ln[K] \qquad \text{(Eq. 2)}$$

To solve for K and n, one of two paths must be taken. Since the data was plotted in the form of nuclear mass as a function of range, the variables M and R must be swapped in Eq. 1 and Eq. 2. Alternatively, the data can be re-plotted with the range as a function of nuclear mass, for which K and n can be easily found from the linear trend line. The trend line from the experimental data for 10.08 GeV, as plotted in Figure 3.1, is:

$$\ln[\text{Nuclear Mass}] = -0.4371(\ln[\text{Range}]) + 5.3089$$

Thus,

$$K = e^{5.3089} = 202.13$$

$$n = -0.4371$$

and

$$M(R) = 202.13R^{-0.4371}$$

Solving for the range as a function of nuclear mass, it can be found that:

$$R(M) = e^{-\frac{1}{0.4371}\ln(\frac{M}{202.13})}$$

and finally

$$R(M) = (\frac{M}{202.13})^{-\frac{1}{0.4371}}$$

3.2.1.2 Radial Range and Straggling Analysis

It was noted that the radial and lateral ranges and straggling followed the same trends as the longitudinal range. Far more variance was observed, particularly at lower energies. A probable cause of this variance, particularly at 20.0 MeV, was found through analyzing the percent energy loss data. For the 1.0 GeV and 10.08 GeV trials, >98.5% and >99.7% of energy loss was due to target ionizations, respectively, for all incident ions tested. However, for heavier ions with 20.0 MeV, a significant portion of the energy loss was due to recoil ionizations, with a maximum of 22.65% observed with incident lead ions. This portion of incident ion energy loss was notably

less for the lower-weight nuclei, with only 0.02% of the energy being lost to recoil ionizations for incident hydrogen ions. These recoil ionizations for lower energy incident ions contribute to the increased variance in all range parameters, compared to the higher energy 1.0 GeV and 10.08 GeV trials. Neither of them suffers from significant recoil events of any kind. The reason for this is that the target cross-section is significantly smaller for high-energy incident ions, reducing the chances for a recoil event to occur. However, as the energy of an incident ion decreases to several MeV, the cross-sections of the target elements and molecules are significantly larger. This explains why recoil events comprise a larger fraction of the incident ion energy loss at 20.00 MeV.

3.2.2 Ionizations

The graphical representation of target ionizations from the target ionizations per incident ion analysis for nuclei at the three noted energy ranges is presented in Figures 3.3 to 3.5.

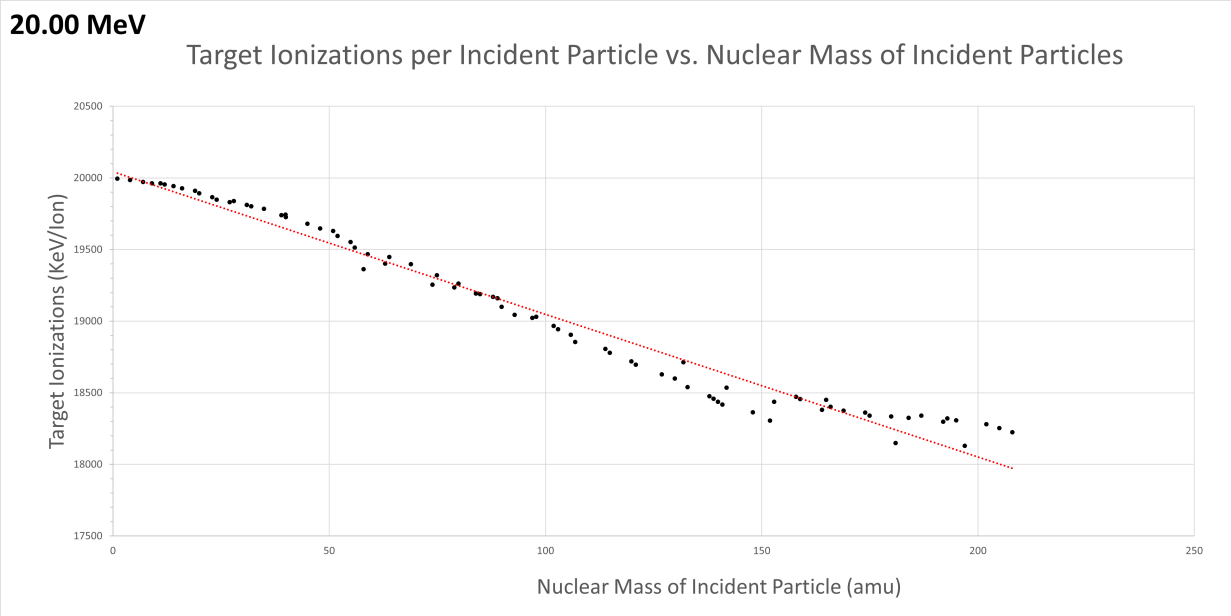

Figure 3.3: Ionization to Tissue from Incident Particles, Ionization Data - 20.00 MeV

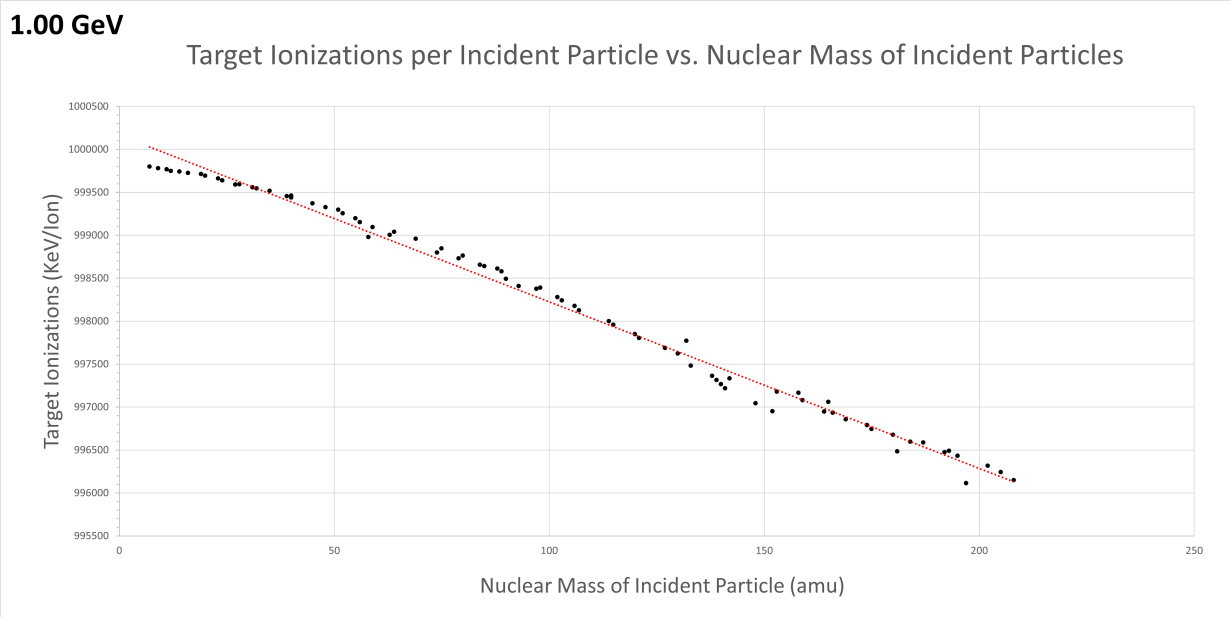

Figure 3.4: Ionization to Tissue from Incident Particles, Ionization Data - 1.00 GeV

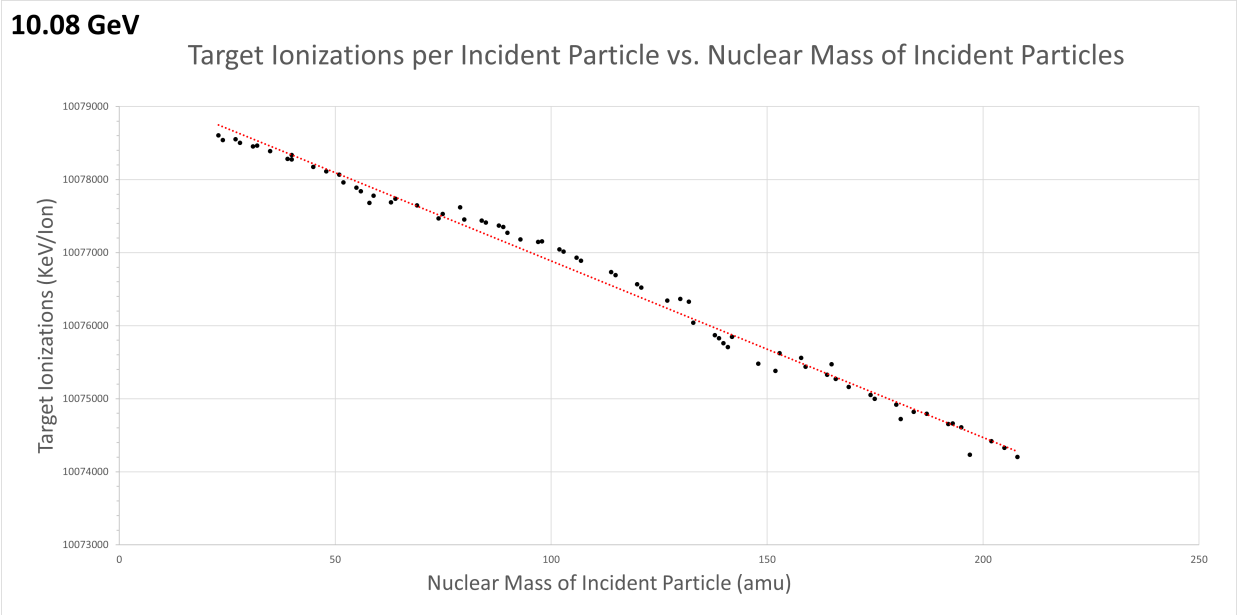

Figure 3.5: Ionization to Tissue from Incident Particles, Ionization Data - 10.08 GeV

It was found that the number of target ionizations per incident ion was relatively constant for all values of Z tested. However, these ionizations did dramatically increase as the incident particle's energy increased. Though the ionizations per incident ion were nearly constant at a given energy level, there was a small correctional coefficient directly proportional to the nuclear mass. This relationship is shown in Eq. 3 below,

$$\text{Ionizations} = \frac{\text{Energy(eV)}}{1000} - \text{K} \qquad \text{(Eq. 3)}$$

where K is the correctional coefficient. For a fixed energy level,

$$\text{K} = \alpha\text{M}$$

where α is the proportionality constant and M is the nuclear mass of the incident ion. It was also found that the accuracy of this approximation significantly increases with the energy level of the incident particle and is slightly greater for lighter particles. Due to the increased accuracy at high energies, such as 10.08 GeV, the correctional coefficient may be ignored when making quick approximations while only sacrificing <0.1% accuracy. However, for more precise measurements, this correctional factor must be accounted for.

3.3 Radiation With Shielding

3.3.1 Polycarbonate Plastic and Metal shielding

Using the astronaut helmet design described in Section 2.4, radiation testing trials were repeated for 20.00 MeV, 1.00 GeV, and 10.08 GeV energy levels of incident particles and for each different helmet coating. The following coatings were tested: gold, lead, platinum, and tungsten. The metal coating is the top layer, followed by the polycarbonate plastic. The model included the helmet coatings followed by the eye layers. A decrease in the total target ionizations per incident ion was observed when compared to the unshielded trials. The maximum change of 0.24% was seen in lead (Z = 82) at 20.00 MeV. The change in ionizations per incident ion decreased with decreasing nuclear mass and increasing energy down to 2.038×10^{-3}% for hydrogen at 10.08 MeV. Similar results were found when replacing the gold coat with lead, platinum, or tungsten.

The change in target ionizations was relatively insignificant for a shielded versus unshielded eye. However, significant changes in radiation interaction were observed for the linear range that each incident particle traveled. Likewise, there were significant differences observed in the total displacements in the target material per incident ion and the total target damage per incident ion. No significant changes were observed to these parameters when exchanging the gold coat with lead, platinum, or tungsten. All four metals performed nearly identically at 500 angstroms of thickness. Gold was often more effective at reducing the range, damage, or displacements that incident particles inflicted by a negligible margin. It was found that at 20.00 MeV, the polycarbonate plastic layer at five millimeters in thickness was sufficient to absorb all nuclei from hydrogen (Z=1) to lead (Z=82), with hydrogen passing a maximum distance of 3660 microns into the material. For 1.00 GeV, the shielding prevented all nuclei from fluorine (Z=9) through lead (Z=82) from penetrating the eye. However, nuclei of lithium (Z=3) through oxygen (Z=8) were still able to penetrate into the eye, whereas nuclei of hydrogen and helium completely passed through the shield, eye, brain, and skull. At an energy level of 10.08 GeV, the polycarbonate and metal shields were sufficient at blocking nuclei of niobium (Z=41) through lead (Z=82) from reaching the eye. However, nuclei of titanium (Z=22) through zirconium (Z=40) were still able to penetrate the shield and implant themselves in the eye. Nuclei of sodium (Z=11) through scandium (Z=21) passed through the eye and implanted in the brain, and nuclei of hydrogen through neon were able to pass completely through the head. A graphical summary of this range data is shown in Figure 3.6 below.

3.3.1.1 Range Analysis

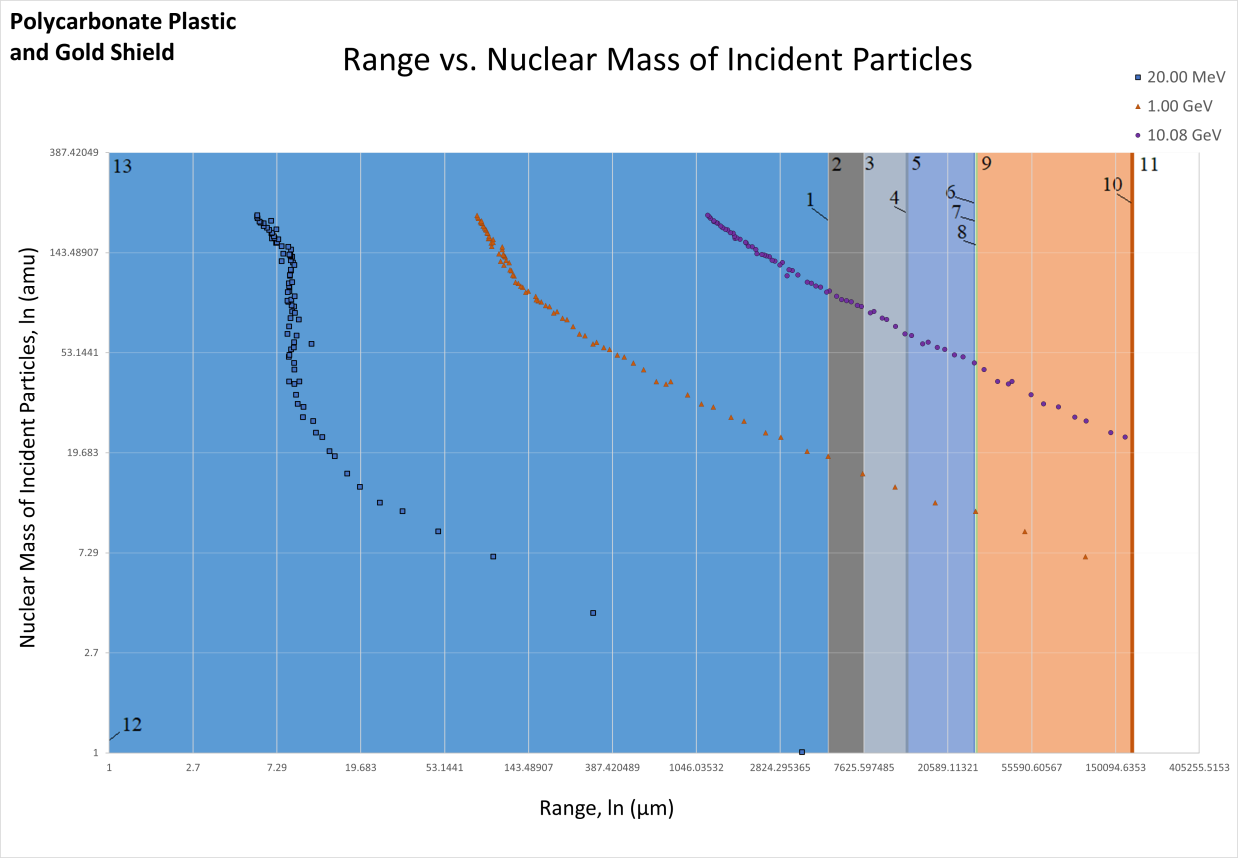

Figure 3.6: Incident Particles Penetrating the Shielded Eye, Range Data

Aside from a large portion of the ions being retained in the polycarbonate plastic layer, the particle ranges for this set of trials reflect trends analogous to those observed in Figure 3.1. It was found that the absolute ranges for particles passing through the polycarbonate plastic layer were slightly lower than those in Section 3.2.1. Note that the elements with ranges greater than the combined thickness of the shield, eye, brain, and skull are not shown in Figure 3.6. These study cases are outside of the scope of this research.

3.3.2 Polycarbonate Plastic, Lead, and Aluminum Shielding

Due to the insignificant variances in shielding efficacy between lead, gold, platinum, and aluminum, a thicker shielding plate made of lead was chosen to comprise the main shielding layer of this new radiation-shielded helmet design for its cost-effectiveness. This shielding design was found to be more effective than the standard design at protecting the eye from high-energy incident nuclei. At 20.00 MeV, results mirrored those of the polycarbonate plastic and metal trials of Section 3.3.1 at 20.00 MeV, with all incident ions from Z = 1 to Z = 82 being absorbed by the polycarbonate plastic layer. At 1.00 GeV, again, ions of fluorine through lead were absorbed by the polycarbonate plastic. However, with this new shielding design, carbon, nitrogen, and oxygen were also retained in the lead shielding layer. Only lithium, beryllium, and boron were able to penetrate and implant themselves into the eye tissue, and hydrogen and helium passed completely through the shield, eye, brain, and skull. These ions that completely passed through the head had minimal interactions with the tissue itself. Perhaps the most notable difference between this shielding design and that of Section 3.3.1 was the difference in damage absorption for the 10.08 GeV trials. Ions of zirconium (Z = 41) through lead (Z = 82) were retained by the polycarbonate plastic layer, as seen in Section 3.3.1. Manganese (Z=25) through yttrium (Z=39) were also successfully retained in the lead layer. Titanium, vanadium, and chromium were retained in the innermost aluminum layer. As a consequence of the increased thickness of this new shielding design and its effectiveness at slowing high-energy incident particles, ions of argon (Z=18) through scandium (Z=21) were now able to implant themselves in the eye tissue. Additionally, ions of sodium (Z = 11) through chlorine (Z=17) were able to pass through the eye and implant themselves in the brain. Many of these ions had passed through the head for the trials in section 3.3.1. Nuclei of hydrogen (Z = 1) through neon (Z = 10) could still pass entirely through the head. A graphical summary of this range data is shown in Figure 3.7 below.

3.3.2.1 Range Analysis

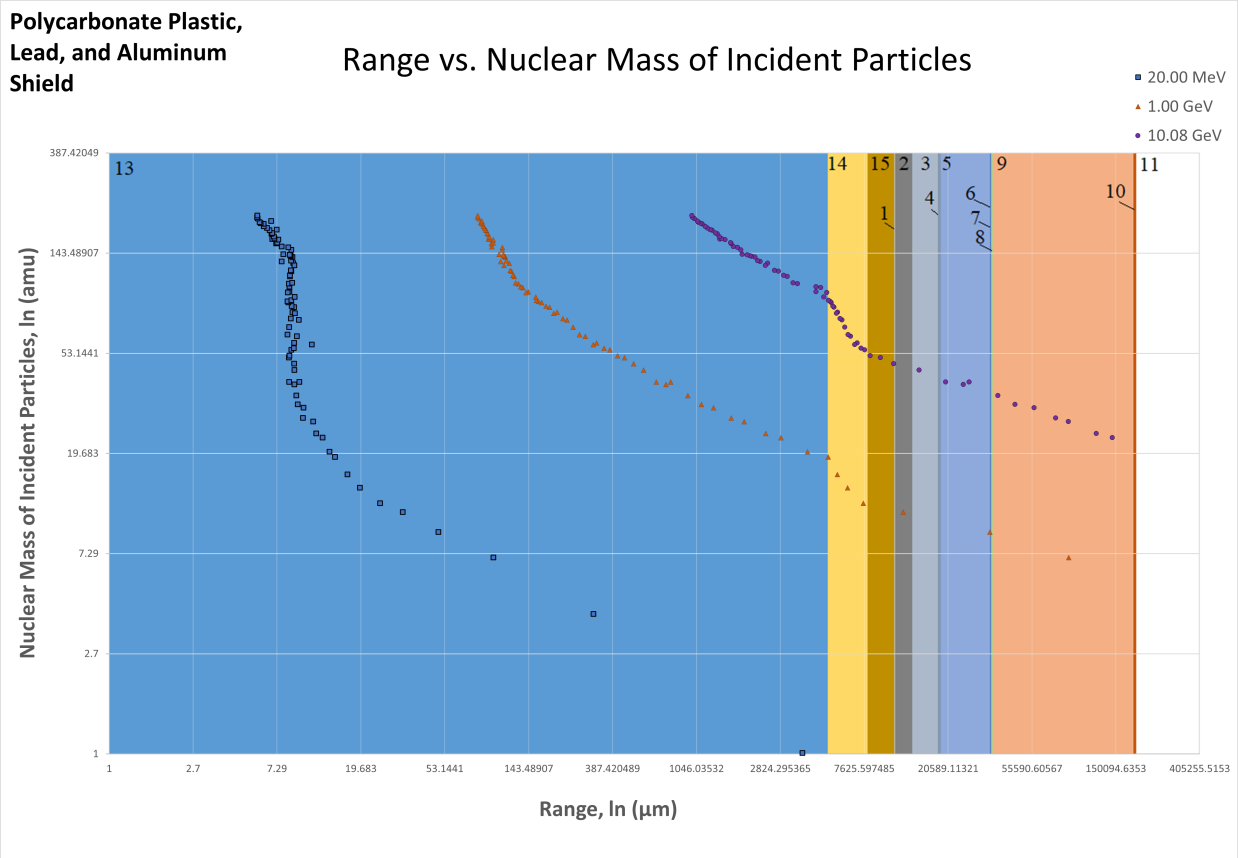

Figure 3.7: Incident Particles Penetrating the Shielded Eye, Range Data

An interesting trend was noted in the lead shielding layer, Layer 14. The slope of the logarithmic rate of particle attenuation increases considerably for particles stopped in or passing through the lead shielding. This observation suggests that lead was more effective at absorbing the energy of ionic radiation than any other material present, such as polycarbonate plastic, aluminum, or organic tissue. As a result, this lead-plated shielding design was also more effective than the gold-plated polycarbonate plastic design at preventing high-energy cosmic rays from penetrating through to the eye. The study was done only for elements with ranges within the target's thickness (shield, eye, brain, and skull). The results are presented in Figure 3.7.

3.3.3 Tissue Damage

The graphical representation of damage from the damage-per-ion analysis for nuclei at the three noted energy ranges is presented in Figures 3.8 to 3.12. This data is graphed with the corresponding damage transmitted to the eye in each shielded setup as well. To determine the amount of damage taken by the eye with shielding present, all three energy trials were conducted with the shield layer in front of the eye and then with the shield layer alone. By subtracting the damage dealt with the shield layer alone from the damage dealt with both the shield and the eye, the damage to the eye alone with the shielding layer present was found. By comparing the damage to the eye for each of the three environments tested, the efficacy of each shielding type was determined.

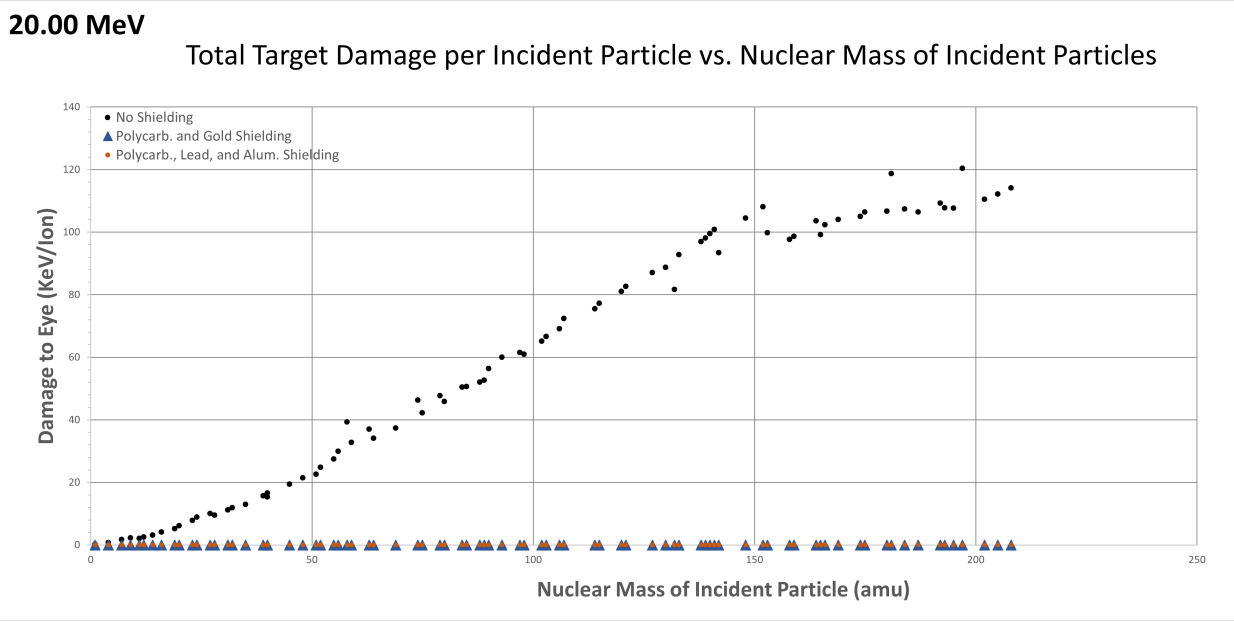

Figure 3.8: Damage to Tissue from Incident Particles, Damage Data - 20.00 MeV

At 20.00 MeV, it was found that the damage to the eye without a shield present is proportional to the nuclear mass of the incident ion. However, incident ions with a nuclear mass larger than approximately 155 amu require a correction to this proportionality. This is because they dealt less

damage than predicted by the proportionality coefficient found for incident ions less than 155 amu. With the 5 millimeters of polycarbonate plastic, all incident particles of Z = 1 to Z = 82 were stopped in the shield. Thus, no damage was dealt to the eye for any of these incident ions, which is reflected in the graph above.

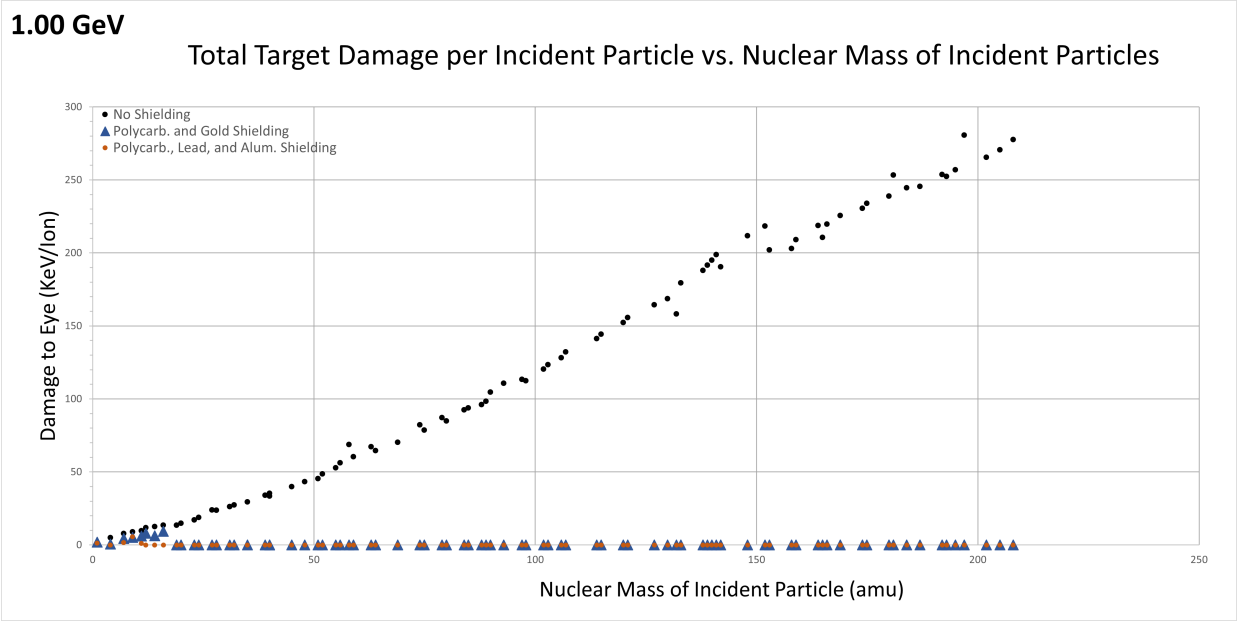

Figure 3.9: Damage to Tissue from Incident Particles, Damage Data - 1.00 GeV

The damage from incident ions at 1.00 GeV also followed a direct proportionality. However, this trend was followed for all ions tested, not just those up to 155 amu, as seen at 20.00 MeV. Both shielding types were successful at absorbing the majority of incident ions tested. However, several light ions were able to penetrate through the shielding. To better illustrate this, Figure 3.5 shows a close-up of Figure 3.4 for only elements Z = 1 to 8.

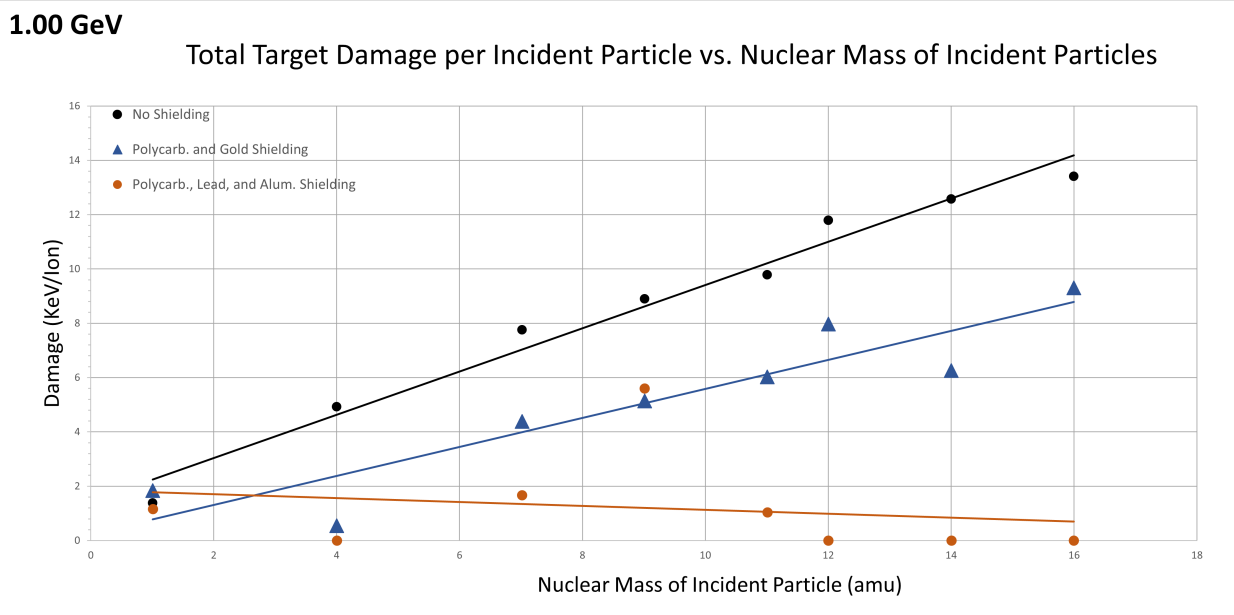

Figure 3.10: Damage to Tissue from Incident Particles, Damage Data - 1.00 GeV (Z = 1 to 8)

At this scale, the differences between the two shielding types became more noticeable. The lead-plated shielding design was able to prevent elements Z = 6 to Z = 8 from penetrating the eye, whereas the polycarbonate and gold shield did not. Both shielding types were effective at reducing the eye's damage. The lead-plated shielding was slightly more effective than the other shielding. The polycarbonate plastic and gold shield design completely absorbed all damage from incident ions of elements Z = 9 to Z = 82, and it absorbed an average of 44.1% of the damage from elements Z = 1 to Z = 8. The lead-plated shield completely absorbed all damage from incident ions of elements Z = 6 to Z = 82, and it absorbed an average of 73.0% of the damage from elements Z = 1 to Z = 5.

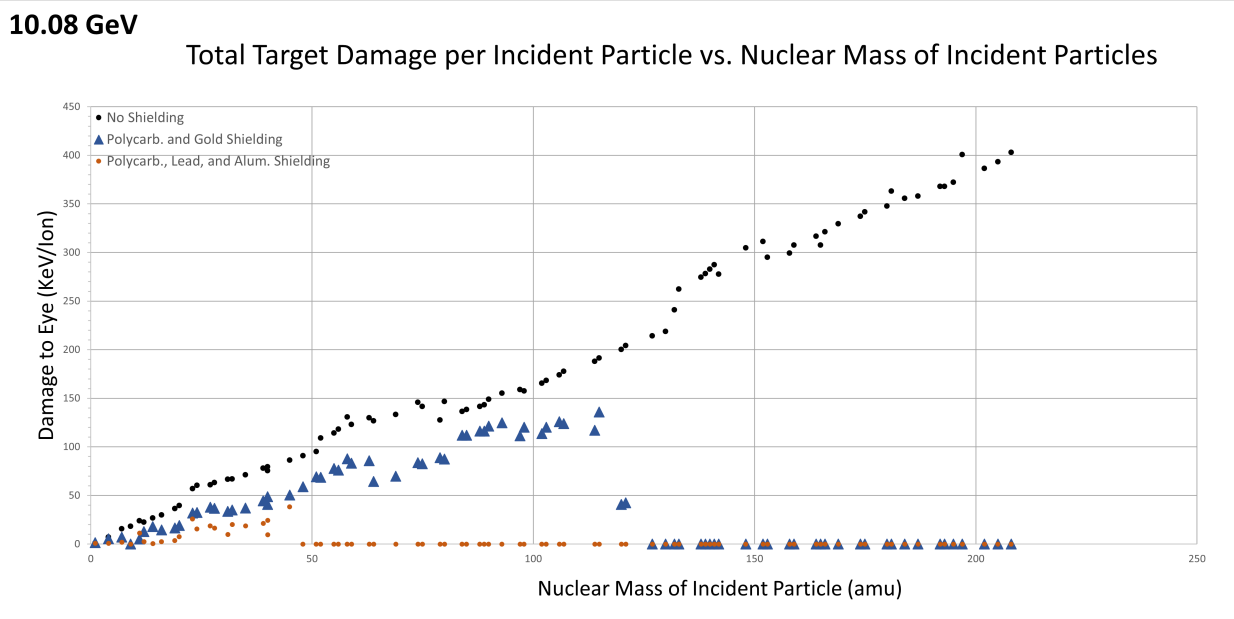

Figure 3.11: Damage to Tissue from Incident Particles, Damage Data - 10.08 GeV

The difference in how well the shielding designs prevent damage to the eye for the energy levels tested was most apparent at 10.08 GeV. It was found that at this energy level the lead-plated design was significantly better at preventing damage to the eye, especially from medium-weight ions, when compared to the polycarbonate plastic and gold design. It was found that the polycarbonate plastic and gold shield design absorbed an average of 62.2% of the damage per amu from incident particles across all elements tested. However, the lead-plated shield absorbed an average of 94.9% of damage per amu from the incident particles across all elements tested, outperforming the polycarbonate plastic and gold shielding by a wide margin. Furthermore, the plastic and gold were only able to prevent elements of Z = 41 to Z = 82 from penetrating the eye, whereas the lead-plated shield prevented elements of Z = 21 to Z = 82 from ever reaching the eye.

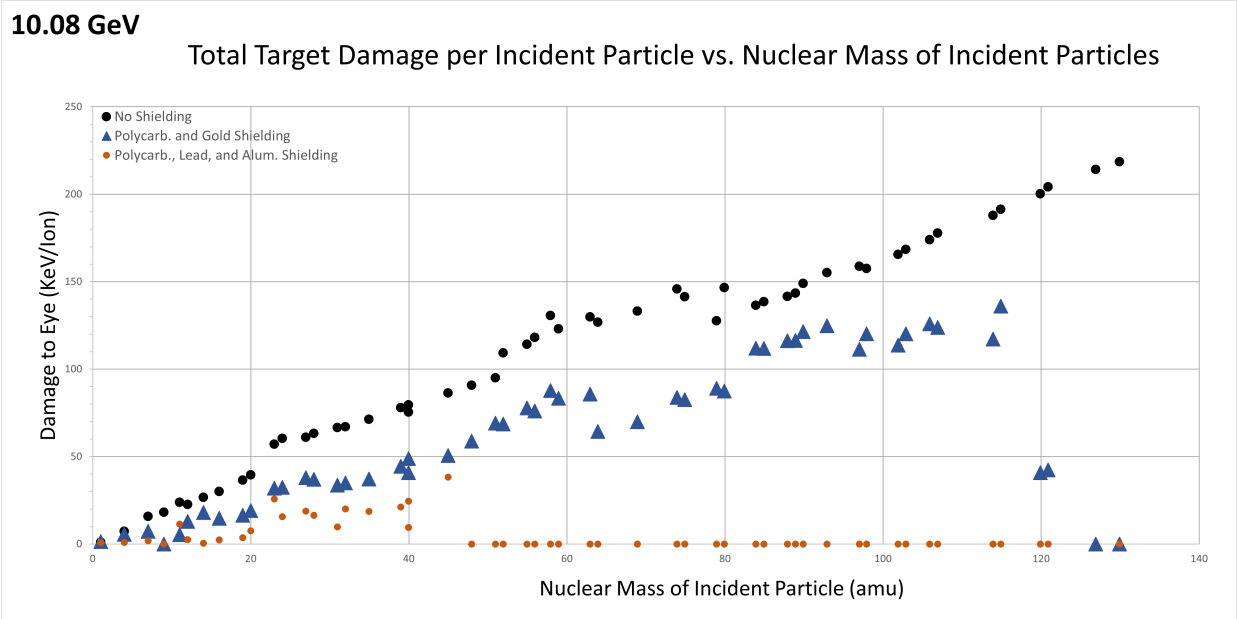

Figure 3.12: Damage to Tissue from Incident Particles, Damage Data - 10.08 GeV (Z=1 to 23)

When only considering the elements that passed through both types of shielding, it was found that the polycarbonate plastic absorbed an average of 46.3% of damage from incident ions of Z = 1 to Z = 21. However, the lead-plated design absorbed an average of 80.2% of damage from incident ions of Z = 1 to Z = 21, outperforming the plastic and gold shielding design by an even wider margin than the 1.00 GeV trials. Thus, it was determined that for high-energy incident ions above 1.00 GeV, the lead-plated shielding design is significantly better at protecting the eye from damage than the polycarbonate plastic and gold shield alone.

4. CONCLUSION

Over the course of this project, the interactions of cosmic rays with eye tissue were simulated using the Monte-Carlo-based software TRIM. These interactions were studied at the broad energy range of cosmic rays and focused on three energy levels: 20.00 MeV, 1.00 GeV, and 10.08 GeV. The logarithmic dependence of cosmic ray range on the nuclear mass of the particles was observed. This relationship increased in accuracy as the mass of the incident particle decreased and energy increased. The damage per incident particle was found to be directly proportional to the nuclear mass. It was noted that the change in damage per incident particle as a function of nuclear mass is more accurate for higher energy levels. The number of total target ionizations per incident particle was found to be relatively constant with respect to nuclear mass. However, a small correctional coefficient was required for accurate prediction of the total target ionizations per incident particle. This correctional coefficient was directly proportional to nuclear mass. The number of total target ionizations per incident particle was found to be strongly dependent on the energy level of the incident particle. Similar trials were conducted using a traditional astronaut helmet design. The results were compared to the new suggested lead-plated shielding design. It was found that at 20.00 MeV, there was no difference in the shielding type; all incident particles were absorbed in the five-millimeter polycarbonate plastic layer. At 1.00 GeV, the lead-plated shield was slightly more effective at absorbing the damage from the few lower-weight elements that were able to pass into the eye. Likewise, due to its thicker design, it was able to retain slightly more elements than the standard astronaut helmet design. However, at 10.08 GeV, it was found that the lead-plated design was significantly more effective at both absorbing the damage of light-weight elements that passed through the shield and at stopping more nuclei from ever interacting with the eye tissue. This is largely the result of lead's ability to attenuate nuclear radiation at a greater rate than polycarbonate plastic, aluminum, or eye tissue. Though this shield design was significantly better at shielding light-weight, high-energy cosmic rays from the eye, it still failed to shield the

eye from significant damage at energies higher than 1.00 GeV. Though the damage per incident particle was shown to decrease as nuclear mass decreases, the intensity of cosmic rays for a given element increases exponentially as the nuclear mass decreases. Thus, it is the lightweight nuclei that pass through both shielding designs at high energies that still pose a considerable risk. Furthermore, utilizing a thicker shielding design would obstruct vision. To avoid compromising on shielding efficiency, it was suggested that a camera and screen design, similar to a VR-headset, be incorporated to enable visibility with this thicker shielding. It is recommended that the efficacy of electromagnetic shielding be explored, potentially in combination with a lead-plated shielding design, as a way to entirely repel these high-energy nuclei. Due to the large penetrating ranges observed for many of the high-energy particles, it is recommended that further analysis be done to determine the interactions and damage that high-energy cosmic rays have on other sensitive organs within the body, even those covered under several suit layers, skin, and muscle.

REFERENCES

[1] F. A. Cucinotta *et al.*, "Space radiation and cataracts in astronauts," *Radiation Research*, vol. 150, pp. 460–66, 2001.

[2] C. Aleci, "From international ophthalmology to space ophthalmology: The threats to vision on the way to moon and mars colonization," *Int Ophthalmology*, vol. 40, pp. 775–86, 2020.

[3] J. F. Ziegler, M. D. Ziegler, and J. P. Biersack, "Srim – the stopping and range of ions in matter," *Defense Technical Information Center*, 2010.

[4] M. Ohishi, T. Yoshikoshi, and T. Yoshida, "A monte carlo simulation study for cosmic-ray chemical composition measurement with cherenkov telescope array," *Presented at the 35th International Cosmic Ray Conference*, Bexco, Busan, Korea, September 19, 2017.

[5] P. Tinyakov, "Ultra-high energy cosmic rays," *Les Houches*, vol. 84, pp. 537–639, 2006.

[6] J. J. Beatty, J. Matthews, and S. P. Wakely, "28. cosmic rays," *Particle Data Group*, 2015.

[7] E. Iyamu, J. Iyamu, and C. I. Obiakor, "The role of axial length-corneal radius of curvature ratio in refractive state categorization in a nigerian population," *ISRN Ophthalmol*, vol. 2011, pp. 1–6, 2011.

[8] *Ever Wondered How Hard Does An Astronaut Have To Bang To Break Glass Of His Helmet?*, Wonderful Engineering, Jan. 2020. [Online]. Available: https://wonderfulengineering.com/strength-astronaut-helmet-glass/.

[9] R. Langley, "Gold coatings for temperature control in space exploration," *Gold Bulletin*, vol. 4, pp. 62–66, 1971.

[10] D. Z. Reinstein *et al.*, "Epithelial thickness in the normal cornea: Three-dimensional display with very high frequency ultrasound," *Journal of refractive surgery*, vol. 24, pp. 571–81, 2008.

[11] *Structure of Type II collagen fragment (C65H102N18O21)*, Mol-Instincts, Sep. 2019. [Online]. Available: https://www.molinstincts.com/structure/type-II-collagen-fragment-cstr-CT1106429248.html.

[12] V. Choh, X. Su, C. Vesco, and J. Fleming, "Densities of bovine ocular components," *Investigative Ophthalmology and Visual Science*, vol. 50, p. 5564, 2009.

[13] D. K. Roberts *et al.*, "Anterior chamber depth, lens thickness, and related measures in african american females with long anterior zonules: A matched study with control for refractive error," *Journal of glaucoma*, vol. 25, pp. 45–8, 2016.

[14] *Water Density*, U. S. Geological Survey, Oct. 2019. [Online]. Available: https://www.usgs.gov/special-topic/water-science-school/science/water-density?qt-science_center_objects=2qt-science_center_objects.

[15] Y. Chen, H. Zhao, P. Schuck, and G. Wistow, "Solution properties of γ-crystallins: Compact structure and low frictional ratio are conserved properties of diverse γ-crystallins," *Protein science: a publication of the Protein Society*, vol. 23, pp. 76–87, 2014.

[16] C. Leung *et al.*, "Comparisons of anterior segment biometry between chinese and caucasians using anterior segment optical coherence tomography," *The British Journal of Ophthalmology*, vol. 94, pp. 1184–9, 2010.

[17] *Actinomycin D*, National Center for Biotechnology Information, Mar. 2005. [Online]. Available: https://pubchem.ncbi.nlm.nih.gov/compound/2019.

[18] H. B. Panitch, K. S. Deoras, M. R. Wolfson, and T. H. Shaffer, "Maturational changes in airway smooth muscle structure-function relationships," *Pediatric Research*, vol. 31, pp. 151–56, 1992.

[19] J. H. Kim *et al.*, "Comparison of individual retinal layer thicknesses between highly myopic eyes and normal control eyes using retinal layer segmentation analysis," *Scientific Reports*, vol. 9, 2019.

[20] H. Kolb, R. Nelson, E. Fernandez, and B. Jones, *Webvision: The Organization of the Retina and Visual System*, Webvision, Oct. 2011. [Online]. Available: https://webvision.med.utah.edu/book/part-i-foundations/simple-anatomy-of-the-retina/.

[21] *Rhodopsin Epitope Tag*, National Center for Biotechnology Information, Jun. 2018. [Online]. Available: https://pubchem.ncbi.nlm.nih.gov/compound/134611628.

[22] X. N. Wang, S. T. Li, W. Li, and Q. Wu, "The thickness and volume of the choroid, outer retinal layers and retinal pigment epithelium layer changes in patients with diabetic retinopathy," *International Journal of Ophthalmology*, vol. 11, pp. 1957–62, 2018.

[23] D. L. Nickla and J. Wallman, "The multifunctional choroid," *Progress in Retinal and Eye Research*, vol. 29, pp. 144–68, 2010.

[24] *What does blood do?*, Institute for Quality and Efficiency in Health Care, Aug. 2019. [Online]. Available: https://www.ncbi.nlm.nih.gov/books/NBK279392/.

[25] S. Vurgese, S. Panda-Jonas, and J. Jonas, "Scleral thickness in human eyes," *PLoS One*, vol. 7, 2012.

[26] T. Pradeep, D. Mehra, and P. H. Le, "Histology, eye," *StatPearls*, 2020.

[27] T. W. Barber, J. A. Brockway, and L. S. Higgins, "The density of tissues in and about the head," *Progress in Retinal and Eye Research*, vol. 46, pp. 85–92, 1970.

[28] H. Li *et al.*, "Investigation of the critical geometric characteristics of living human skulls utilising medical image analysis techniques," *International Journal of Vehicle Safety*, vol. 7, pp. 199–208, 2014.

[29] *Hydroxyapatite*, National Center for Biotechnology Information, Aug. 2005. [Online]. Available: https://pubchem.ncbi.nlm.nih.gov/compound/Hydroxyapatite.

[30] J. S. Al-Sanabani, A. A. Madfa, and F. A. Al-Sanabani, "Application of calcium phosphate materials in dentistry," *International Journal of Biomaterials*, 2013.

[31] T. L. Brown and H. E. Lemay, *Chemistry: The Central Science*, 10th ed. New York, NY, USA: Pearson/Prentice-Hall, 2005.

[32] *Polycarbonate Properties*, World of Chemicals, 2021. [Online]. Available: https://www.worldofchemicals.com/chemicals/chemical-properties/polycarbonate.html.

[33] *Polycarbonate*, International Polymer Solutions Inc., Feb. 2019. [Online]. Available: https://www.ipolymer.com/pdf/Polycarbonate.pdf.

APPENDIX A: EYE MODEL

Eye Composition and Characteristics by Layer:

1. Cornea:
    - Thickness: 53.4 μm [10]
    - A simplified model of this layer was used, which was comprised of type-II collagen.
    - Molecular Formula: $C_{65}H_{102}N_{18}O_{21}$ [11]
    - Density: 1.058 g/cm^3 [12]
2. Anterior Chamber:
    - Thickness: 2.57 mm [13]
    - This layer is filled with aqueous humor, which was simplified to be water.
    - Molecular Formula: H_2O
    - Density: 0.99414 g/cm^3 (Water at body temperature) [14]
3. Lens:
    - Thickness: 4.83 mm [13]
    - The lens is primarily composed of crystalline proteins [13]. These proteins do not have a specifically determined molecular formula. Because they are polypeptide chains, similar to collagen, a simplified model of this layer was used with proteins containing a molecular formula similar to that of type-II collagen.
    - Molecular Formula: $C_{65}H_{102}N_{18}O_{21}$ [15]
    - Density: 1.098 g/cm^3 [12]

4. Iris:

    - Thickness: 0.43 mm [16]
    - The iris is made almost entirely of smooth muscle fibers. It was assumed that these are made of actinomyosin, an actin-myosin complex.
    - Molecular Formula: $C_{62}H_{86}N_{12}O_{16}$ [17]
    - Density: 1.05 g/cm^3 [18]

5. Vitreous Body:

    - Thickness: 15.17 mm [13]
    - This layer is filled with Vitreous Humor, which was simplified to be water.
    - Molecular Formula: H_2O
    - Density: 0.99414 g/cm^3 (Water at body temperature) [14]

6. Retina:

    - Thickness: 265.00 μm [19]
    - A simplified model was used, where it was assumed that this layer was composed of rods, since rods outnumber cones 20:1 [20]. It was also assumed that rods are entirely comprised of rhodopsin.
    - Molecular Formula: $C_{37}H_{62}N_{10}O_{16}$ [21]
    - Density: 1.034 g/cm^3 [12]

7. Choroid:

    - Thickness: 280.00 μm [22]
    - This layer is primarily comprised of vascular tissue [23]. This layer was simplified to be made entirely of blood vessels. It was assumed that these blood vessels were primarily comprised of blood. Blood is 55% blood plasma and 45% blood cells, blood

plasma is 90% water and 10% proteins, and blood cells are approximately 70% water and 30% cellular proteins, lipids, and nucleic acids [24].

- Atomic Composition: 63.19% H, 28.47% O, 6.67% C, 1.67% N.
- Density: 1.034 g/cm^3 [12]

8. Sclera:

   - Thickness: 0.65 mm [25]
   - This layer is dense and primarily made of type-II collagen[26].
   - Molecular Formula: $C_{37}H_{62}N_{10}O_{16}$ [11]
   - Density: 1.077 g/cm^3 [12]

9. Brain:

   - Thickness: 150.00 mm
   - A simplified model was used, which assumes this layer to be entirely made of a simplified average protein composition.
   - Molecular Formula: $C_{32}H_{50}N_8O_{10}$
   - Density: 1.100 g/cm^3 [27]

10. Skull:

    - Thickness: 7.00 mm (based on averages found in Li and colleagues' research article [28])
    - A simplified model was used, which assumed this layer to be entirely made of hydroxyapatite.
    - Molecular Formula: $Ca_{10}(PO_4)_6OH_2$ [29]
    - Density: 3.156 g/cm^3 [30]

APPENDIX B: SHIELDING

Shielding Materials: NASA Helmet Design

1. Gold Coating:
    - Thickness: 500 Å [9]
    - Density: 19.32 g/cm^3 [31]
2. Polycarbonate Plastic:
    - Thickness: 5.00 mm [8]
    - Molecular Formula: $C_{16}H_{16}O_4$ [32]
    - Density: 1.2 g/cm^3 [33]

Metals tested instead of gold:

1. Platinum:
    - Thickness: 500 Å
    - Density: 21.45 g/cm^3 [31]
2. Tungsten:
    - Thickness: 500 Å
    - Density: 19.35 g/cm^3 [31]
3. Lead:
    - Thickness: 500 Å
    - Density: 11.35 g/cm^3[31]

Shielding Materials: Lead-Plated Shield Design

1. Polycarbonate Plastic:
    - Thickness: 5.00 mm [8]
    - Molecular Formula: $C_{16}H_{16}O_4$ [32]
    - Density: 1.2 g/cm^3 [33]
2. Lead:
    - Thickness: 3.00 mm
    - Density: 11.35 g/cm^3[31]
3. Aluminum:
    - Thickness: 3.00 mm
    - Density: 19.35 g/cm^3 [31]